The Effects of Interfacial Particles on the Contact of an Elastic Sphere With a Rigid Flat Surface

Dinçer Bozkaya
Graduate Student

Sinan Müftü
Associate Professor
Fellow ASME

Department of Mechanical Engineering,
Northeastern University,
Boston, MA 02115

In chemical mechanical polishing (CMP), a rigid wafer is forced on a rough elastomeric polishing pad, while a slurry containing abrasive particles flows through the interface. One of the important factors that influence the material removal rate in CMP is the magnitude of contact force transmitted to the abrasive particles trapped at the contact interface. The total push-down force is distributed to the direct contact between the wafer and the pad, and to the three-body contact between the wafer, the pad, and the abrasive particles. The presence of the abrasive particles alters the asperity contact, which otherwise can be described by Hertz contact relationships. In this study, the effect of the interfacial particles on the single asperity contact is investigated. An approach used by Greenwood and Tripp (1967, "The Elastic Contact of Rough Spheres," ASME J. Appl. Mech., ***34****, pp. 153–160) to study the contact of rough spheres is utilized since the presence of the particles provides a rough character to the contact. The results show that the contact behavior becomes non-Hertzian with decreasing contact force and increasing elastic modulus, particle size, and particle concentration. The role of the interfacial particles is to spread the contact over a larger area while lowering the maximum contact pressure at the center of contact predicted by Hertz contact. The conditions required to transfer the contact force on the particles effectively are also described.*
[DOI: 10.1115/1.2958073]

Keywords: chemical mechanical polishing, particles, rough contact, spherical contact

1 Introduction

Chemical mechanical polishing (CMP) is a manufacturing process commonly used in planarization of wafer based integrated circuits (ICs). CMP is a key technology in generating planar surfaces for interlevel dielectric (ILD), shallow trench isolation (STI), and damascene metallization [1]. The introduction of the new materials such as porous ultra-low-*k* dielectrics and shrinking device sizes calls for more stringent requirements for the CMP process to control the material removal rate (MRR) and planarity. CMP involves pushing down a rotating wafer attached to a wafer-carrier, against a rotating polishing pad while liquid slurry, containing various oxidizing chemicals and abrasive particles, is supplied to the pad-wafer interface. The global equilibrium of the wafer is established between the forces exerted by the lubrication layer due to the slurry, contact, and deformation of the pad, and the term *soft elastohydrodynamic* lubrication has been coined for the problem that defines the wafer-scale force equilibrium [2]. The problem can be investigated in a hierarchical manner of which the present work covers the three-body and two-body contacts at the particle, wafer, and pad interfaces. Improvements in the CMP outcomes can be facilitated if the complex relationships between various processing conditions and their effect on the MRR can be understood.

The chemical reactions between the CMP-slurry and the wafer are the primary driver for preparing the surface for polishing. The contact of the particles at the pad-wafer interface provides the mechanism to remove the material from the wafer surface [3]. The elastic modulus of the wafer and abrasive particles is large compared to the elastic modulus of the pad [1]. Therefore the wafer and abrasive particles can be considered to be rigid in a model of the pad-wafer interface. The pad is made of an elastomeric material (e.g., polyurethane), which exhibits hyperelastic material behavior [4]. The wafer is smooth as compared to the pad [5]. Hence the pad-wafer contact can be modeled as the contact of one rigid smooth and one deformable rough surface in the presence of spherical rigid particles trapped at the contact interface.

In general, when two surfaces are brought into contact, the real contact area is only a fraction of the apparent contact area due to the roughness of the surfaces. Initially, contact occurs at the tip of the tallest asperities. As the load is increased, not only the asperities start to deform and flatten, but also the number of asperities in contact increases. As a result, contact spreads to a larger area. One of the common solution methods to approach this problem is the utilization of the statistics of the surface topography. Multi-asperity models fall into this group [6,7]. In the Greenwood and Williamson (GW) model the statistical distribution of the asperity peak heights is used. Each asperity is assumed to have a smooth spherical tip and to deform according to Hertz contact [6]. Hertz contact is limited to small deformation and linear elastic material behavior [8]. The contact of a single pad asperity and a rigid wafer, described in this paper, violates the assumptions of the Hertz contact as the pad material behavior is nonlinear and large deformations occur since the pad is relatively soft. Furthermore, the abrasive particles at the interface become trapped in the contact interface, which influences the single asperity contact behavior. Hertz contact has been widely utilized for the single asperity contact of the pad with the wafer in material removal rate models developed for CMP [3,5,9–11].

Different scales of contact in CMP are illustrated in Figs. 1(*a*)–1(*d*). In this work, a single asperity model is developed for the contact of a deformable pad asperity and a rigid surface, which includes the effects of the rigid spherical particles at the interface. This is represented schematically in Figs. 1(*b*)–1(*d*). The effects of the relative motion of the pad and the wafer, and the effects of the

---

Contributed by the Tribology Division of ASME for publication in the JOURNAL OF TRIBOLOGY. Manuscript received October 1, 2007; final manuscript received June 16, 2008; published online August 4, 2008. Assoc. Editor: Hong Liang. Paper presented at the Materials Research Society, Spring 2007 Conference in San Francisco, CA.

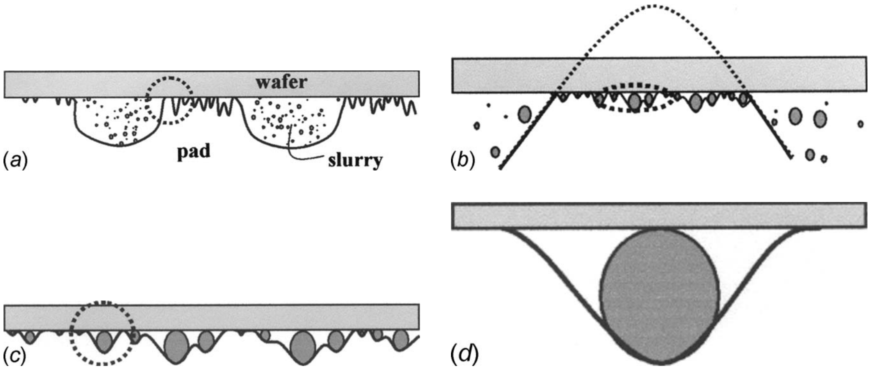

Fig. 1 Cross-sectional view of the wafer-pad interface at different scales of contact

lubrication due to slurry are neglected. At the pad-wafer interface, the contact force could be carried by both direct contact of the pad and the wafer and/or the contact through the entrapped particles (*particle contact*). The particle level interactions are modeled in two steps, *single particle* (SP) model and *multiparticle* (MP) model as shown in Figs. 1(*d*) and 1(*c*), respectively. In the SP model, the contact of a single spherical particle between one rigid and one deformable surface is studied using the finite element (FE) method. Once the contact behavior of a single particle is found, the overall effect of multiple particles on the contact of two flat surfaces (one rigid and one deformable) is modeled. This MP model provides the necessary relationships required to characterize the local contact of *single asperity* in the single asperity (SA) model, as shown in Fig. 1(*b*).

2 Single Particle (SP) Model

Contact mechanics of a rigid spherical particle, with radius r_p, trapped between two flat surfaces, as shown in Fig. 2, is investigated. The separation distance between the surfaces is initially large and the particle is not in contact with the rigid surface (Fig. 2(*a*)). At small loads, the contact is supported by particle contact (Fig. 2(*b*)). When the penetration of the particle becomes sufficiently deep, the flat surfaces come into direct contact. In this paper, the condition where the contact is supported by the particle and the flat surface is called the *mixed contact* (Fig. 2(*c*)). In this regime, an important parameter is the *influence radius* r_i of the particle, which is used to quantify the noncontact region around the particle. Also note that, due to the reasons that will become clear shortly, the deformation in the particle contact regime is characterized with respect to the penetration of the particle δ_p, but the deformation in the mixed contact regime is characterized with respect to the average compressive strain $\varepsilon_s = \delta_d / t_s$, where $\delta_d (= \delta_p - 2r_p)$ is the displacement of the deformable medium.

This problem is investigated with an axisymmetric finite element model, using ANSYS 9.0 (Canonsburg, PA). The outer radius r_o of the deformable domain is taken as $200r_p$, which is sufficiently large to ensure that the results do not depend on this parameter. The thickness of the deformable medium t_s, however, affects the particle and direct contact as the particle becomes completely embedded in the deformable medium. The model is run using $t_s = 250r_p$, $500r_p$, and $1000r_p$ for a total average compressive strain ε_s of the deformable medium of 0.45. It is confirmed that the results presented in this section are independent of t_s. In the FE model, the nodes attached to the particle and the rigid surface are coupled and displaced incrementally toward the deformable medium to a final displacement of $\delta_p = 227r_p$, or $\varepsilon_s = 0.45$ when $t_s = 500r_p$. The model consists of 71,000 four-noded axisymmetric elements (PLANE182), by using the nonlinear finite deformation definition (NLGEOM command). The mesh in the vicinity of the particle is finer and is gradually coarsened away from the particle. Two different frictionless contact pairs for the contact of the particle and the deformable medium, and the rigid surface and the deformable medium are defined with the contact elements (CONTA172) for the deformable medium and rigid target elements (TARGE169) for the rigid particle and the surface. The deformable medium is constrained from the bottom surface in the direction of the particle movement.

Two parameter Mooney–Rivlin hyperelastic material model is used to simulate the material behavior. In this model, the strain energy density function is expressed in terms of two material constants, a_{10} and a_{01} [12]. Here a_{10} and a_{01} are taken to be 0.5 MPa, which yields $E_s = 6$ MPa [13]. Poisson's ratio of the elastic surface, $\nu_s = 0.49$, which is typical for nearly incompressible rubber-like materials, is used in the model [13].

The nondimensional variables used in this work are defined in Table 1. Note that the superscript "*" indicates the nondimensional variables for the SP model and "~" is used for the following MP and SA models. The FE model is solved for each displacement increment, δ_p^*, and the particle contact force, f_p^*, is calculated by summing the forces at the contact nodes attached to the deformable medium in contact with the particle. The force acting on the particle is indicated by f_p^{p*} or f_p^{m*} depending on whether the contact represents the pure particle contact or the mixed contact situations, respectively.

Figure 3 shows the variation of f_p^{p*} in the pure particle contact regime ($0 < \delta_p^* < 2$). Hertz contact is valid for small penetration depths δ_p^*; however, the assumptions of Hertz contact become

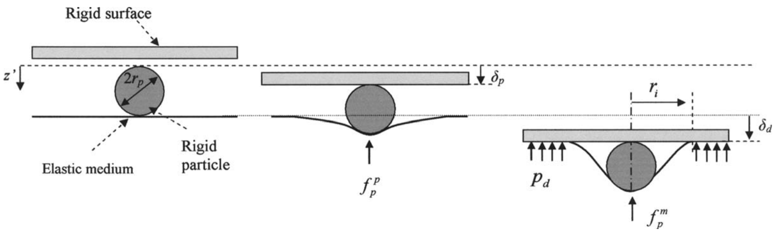

Fig. 2 Single particle model

Table 1 Nondimensional parameters for SP, MP, and SA models

SP model			MP and SA models		
L^*	F^*	P^*	$\tilde{L}$	$\tilde{F}$	$\tilde{P}$
$\dfrac{L}{r_p}$	$\dfrac{F(1-\nu_s^2)}{E_s r_p^2}$	$\dfrac{P(1-\nu_s^2)}{E_s}$	$\dfrac{L^* r_p}{\sigma_p}$	$\dfrac{F^* r_p^2}{\sigma_p^2}$	P^*

invalid, and the error of the particle force predicted by Hertz contact $\left(f_H^*=\frac{4}{3}\delta_p^{*3/2}\right)$ increases up to 20% as δ_p^* approaches 2. A curve fit for the pure particle contact force f_p^{p*} can be described by using a correction term for the Hertz contact as follows:

$$f_p^{p*}(\delta_p^*) = \tfrac{4}{3}\delta_p^{*3/2} - 0.10\delta_p^{*2.89} \quad \text{for } 0 < \delta_p^* < 2 \tag{1}$$

In the mixed contact regime ($\delta_p^* > 2$), the penetration is measured with respect to the deformation of the elastic pad, $\delta_d(=\delta_p-2r_p)$, as depicted in Fig. 2(c), which is nondimensionalized as $\varepsilon_s=\delta_d/t_s$, with respect to the thickness of the deformable medium, t_s. This gives a measure of the average compressive strain in the deformable medium. In this contact regime, the rate of increase in the contact force on the particle f_p^{m*} is smaller as shown in Fig. 3 due to the influence of direct contact. The contact force acting on the particle f_p^{m*} is expressed by using the following curve-fit relation:

$$f_p^{m*}(\varepsilon_s) = \begin{cases} 5.4(\varepsilon_s)^{0.57} + 3.12 & \text{for } 0 < \varepsilon_s < 0.05 \\ 11.1(\varepsilon_s - 0.05)^{0.90} + 4.10 & \text{for } 0.05 < \varepsilon_s < 0.2 \\ 40.94(\varepsilon_s - 0.2)^2 + 13.14(\varepsilon_s - 0.2) + 6.11 & \text{for } 0.2 < \varepsilon_s < 0.45 \end{cases} \tag{2}$$

The force carried by the wafer-to-pad direct contact is determined by using the influence radius, r_i^*, and maximum direct contact pressure, $p_d^{\max*}$. The direct contact pressure p_d^*, varies along the contact interface as shown in Fig. 4(a), for different pad compression ε_s values. The direct contact pressure, p_d^*, is zero at the outer edge of the particle contact region and increases gradually to its maximum, $p_d^{\max*}$. The influence radius r_i^* is corrected to take this transition region into account. The influence radius r_i^* is found by integrating p_d^* over the direct contact interface to find the total direct contact force, which is then used to calculate the correction term to give the same contact force with pressure $p_d^{\max*}$ as

$$r_i^* = \frac{1}{p_d^{\max*}} \int_{r_i'^*}^{r_o} p_d^* dr \tag{3}$$

The influence radius, r_i^* thus found varies with ε_s as shown in Fig. 4(b) and it can be curve-fit to the following relationship:

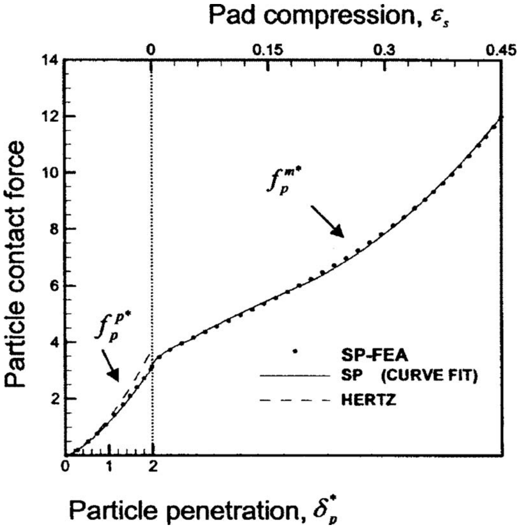

Fig. 3 Particle contact force in pure particle, f_p^{p*}, and mixed, f_p^{m*}, contact regimes obtained by the FE model

$$r_i^*(\varepsilon_s) = 1.52(\varepsilon_s)^{-0.45} \quad \text{for } 0 < \varepsilon_s < 0.45 \tag{4}$$

The maximum contact pressure $p_d^{\max*}$ increases linearly with penetration into the deformable pad for small ε_s values, and it becomes eventually nonlinear at large ε_s as shown in Fig. 4(c). The variation of the maximum contact pressure $p_d^{\max*}$ can be described by the following curve-fit equations:

$$p_d^{\max*}(\varepsilon_s) = \begin{cases} 0.76\varepsilon_s & \text{for } 0 < \varepsilon_s < 0.015 \\ 0.85(\varepsilon_s - 0.015) + 0.011 & \text{for } 0.015 < \varepsilon_s < 0.2 \\ 1.8(\varepsilon_s - 0.2)^{1.16} + 0.17 & \text{for } 0.2 < \varepsilon_s < 0.45 \end{cases} \tag{5}$$

3 Multiparticle (MP) Model

Next, contact of a rigid-flat surface with a deformable-flat surface is considered when there are rigid spherical particles with different sizes entrapped in the interface. Such a condition is depicted in Fig. 5. The mean particle radius, r_μ, the standard deviation of the particle radii, σ_p, and the probability density function (PDF) of the particle radii, $\tilde{\Phi}_p(\tilde{r}_p)$, are assumed to be known. In this interface, the light external forces are transmitted between the two surfaces by particle contacts, and direct contact of the surfaces occurs as the external force is increased. Therefore, the mean contact pressure $\tilde{P}_c$ is defined as follows:

$$\tilde{P}_c = \begin{cases} \tilde{P}_p^p & \text{if } \tilde{d}_{\text{sep}} > 0 \\ \tilde{P}_p^m + \tilde{P}_d & \text{if } \tilde{d}_{\text{sep}} < 0 \end{cases} \tag{6}$$

where $\tilde{d}_{\text{sep}}$ is the separation of the two surfaces as defined in Fig. 5, $\tilde{P}_p^p$ is the mean contact pressure for the pure particle contact regime (Fig. 5(b)), and $\tilde{P}_p^m$ and $\tilde{P}_d$ are the mean contact pressure acting on the particles and the direct wafer-to-pad contact pressure in the mixed contact regime (Fig. 5(c)), respectively. As in the case of the SP model, the contact interactions are characterized with respect to the approach of the two surfaces $\tilde{d}_{\text{sep}}$ in the particle contact regime and with respect to the average compressive strain $\varepsilon_p=d_{\text{sep}}/t_s$ in the direct contact regime. The particle contact regime is computed in the range $0<\tilde{d}_{\text{sep}}<12$, where the upper limit corresponds to $\tilde{r}_\mu+8$. The direct contact regime, which is encoun-

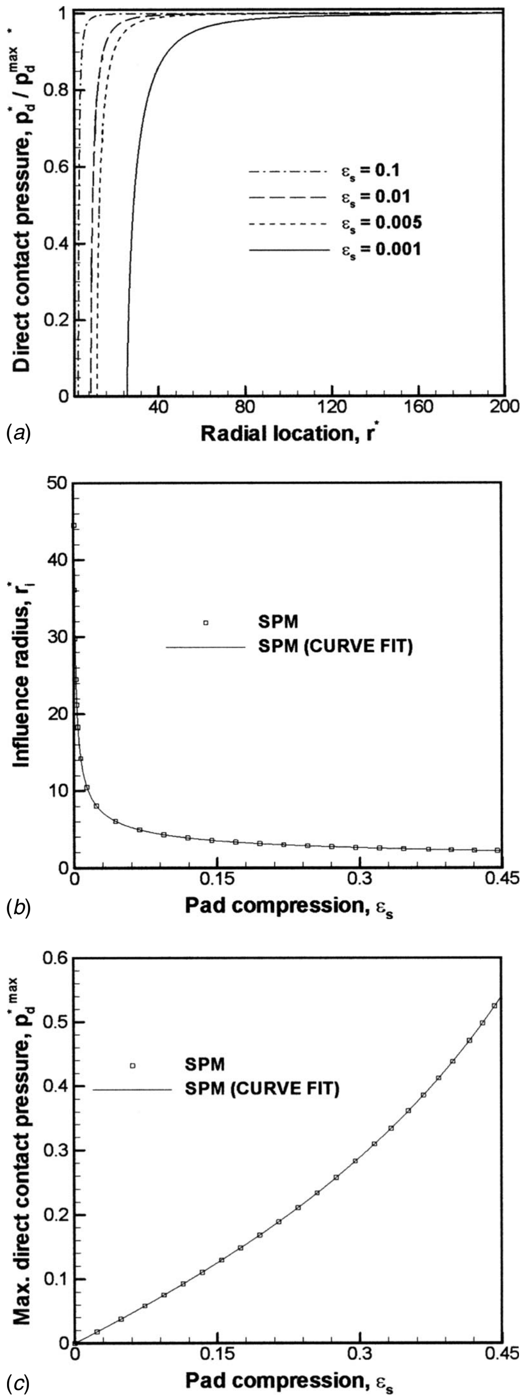

Fig. 4 (*a*) Variation of the direct contact pressure, p_d^*, along the contact interface for different penetration depths, δ_p^*, obtained by FEA. (*b*) Influence radius, r_i^*, and (*c*) maximum direct contact pressure, p_d^{max*}, as a function of pad compression, ε_s, defined by Eqs. (4) and (5), respectively.

tered when $\tilde{d}_{sep} < 0$, is evaluated in the range $-0.45 < \varepsilon_p < 0$. Note that the average compressive strain ε_p is negative in the MP model due to the definition of the $\tilde{d}_{sep}$ as defined in Fig. 5.

3.1 Number of Active Particles.

Only a fraction of the particles in the slurry are trapped between the surfaces and become active in contact at a given separation distance $\tilde{d}_{sep}$ (Fig. 5(*a*)). In the pure particle contact regime, as the separation distance $\tilde{d}_{sep}$ decreases, more particles get trapped between the surfaces and become active (participate) in contact (Fig. 5(*a*)). The particles with diameter ($2\tilde{r}_p$) larger than the separation distance $\tilde{d}_{sep}$ are considered to be captured in the contact interface, whereas smaller particles can move freely between the surfaces [3]. The number of particles per unit area $\tilde{\eta}_a$, which are active in contact, can be found from the volumetric particle concentration $\tilde{\eta}_v$ and the available volume $V\!\!\!/ = A_u\tilde{d}_{sep}$, using $\tilde{\eta}_a = \tilde{\eta}_v V\!\!\!/$ where $A_u = 1$ for unit area. However, one needs to consider that the separation distance at which each particle becomes active is dependent on the size of the particle. Therefore the number of active particles, $\tilde{\eta}_a$, at separation distance, $\tilde{d}_{sep}$, can be obtained by the summation of the $\tilde{\eta}_a$ at larger $\tilde{d}_{sep}$. Using the PDF $\tilde{\Phi}_p(\tilde{r}_p)$ of the particle radii, this summation gives

$$\tilde{\eta}_a(\tilde{d}_{sep}) = \tilde{\eta}_v \int_{\tilde{d}_{sep}/2}^{\infty} 2\tilde{r}_p \tilde{\Phi}_p(\tilde{r}_p) d\tilde{r}_p \qquad (7)$$

In the mixed contact regime, where the pad and the wafer also engage in contact, the number of active particles $\tilde{\eta}_a^m$ is considered to be constant and is calculated by setting $\tilde{d}_{sep} = 0$ in Eq. (7).

The weight particle concentration, η_w, is the common measure used for the slurries and can be converted to the volumetric particle concentration, $\tilde{\eta}_v$, for spherical particles by using the following relationship:

$$\tilde{\eta}_v = \frac{\rho_s}{\rho_p} \frac{\eta_w}{\displaystyle\int_0^{\infty} \frac{4}{3}\pi \tilde{r}_p^3 \tilde{\Phi}_p(\tilde{r}_p) d\tilde{r}_p} \qquad (8)$$

where ρ_p and ρ_s are the mass densities of the particles and slurry, respectively. As a result of the nondimensionalization of the variables in Eqs. (7) and (8), the areal η_a and volumetric η_v particle densities can be nondimensionalized, respectively, as $\tilde{\eta}_a = \eta_a \sigma_p^2$ and $\tilde{\eta}_v = \eta_v \sigma_p^3$.

3.2 Pure Particle Contact Regime.

In the case of contact of two rough surfaces, the GW model shows that the number of asperities that are in contact, n_{asp}, and the mean contact pressure, P_c, between two rough surfaces separated by a distance, d_{sep}, can be found as follows [6]:

$$n_{asp} = \eta \int_{d_{sep}}^{\infty} \Phi_{asp}(z) dz \quad \text{and } P_c = \eta \int_{d_{sep}}^{\infty} f_{asp}(\delta) \Phi_{asp}(z) dz \qquad (9)$$

where $\delta = z - d_{sep}$ is the penetration of each asperity, $f_{asp}(\delta)$ is a function describing the load-displacement behavior of a single asperity, z is the asperity height, $\Phi_{asp}(z)$ is the PDF of the asperity peak heights, and η is the number of asperity peaks per unit area.

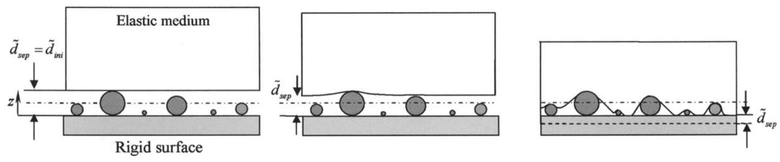

Fig. 5 Multiparticle model

In this work, the contact between particles and two surfaces is modeled by replacing the asperities of the rough surface with interfacial particles. This requires interchanging the asperity height with the particle radius, $z=2r_p$, as shown in Fig. 5. Then, the nondimensional penetration depth of each particle, as defined in the SP model, becomes $\delta_p^*=(2r_p-d_{\text{sep}})/r_p$. By using the number of the active particles $\tilde{\eta}_a(\tilde{d}_{\text{sep}})$ from Eq. (7), the load-displacement function of a single particle in pure particle contact regime f_p^{p*} from Eq. (1), and the PDF of particle radii $\tilde{\Phi}_p$, the mean particle contact pressure $\tilde{P}_p^p$ due to particles caught in the interface of two flat surfaces can be found as follows:

$$\tilde{P}_p^p = \tilde{\eta}_v \int_{\tilde{d}_{\text{sep}}/2}^{\infty} 2\tilde{r}_p \tilde{f}_p^p(\tilde{\delta}_p)\tilde{\Phi}_p(\tilde{r}_p)d\tilde{r}_p \quad \text{for } \tilde{d}_{\text{sep}}>0 \qquad (10)$$

3.3 Mixed Contact Regime. The mean contact pressure $\tilde{P}_p^m$ due to particle contacts in the mixed contact regime ($\tilde{d}_{\text{sep}}<0$) is found in a way similar to Eq. (10), by using Eq. (2) for $\tilde{f}_p^m$, and by taking the lower limit of the integral as 0, as the number of active particles is constant in this regime. Note that the force acting on particles $\tilde{f}_p^m$ in the SP model is expressed in terms of the average compressive strain of the deformable medium, which becomes $\varepsilon_p=d_{\text{sep}}/t_s$ in the mixed contact regime of the MP model. The mean contact pressure $\tilde{P}_p^m$ due to particle contacts in the mixed contact regime is then found as follows:

$$\tilde{P}_p^m = \tilde{\eta}_v \int_0^{\infty} 2\tilde{r}_p \tilde{f}_p^m(-\varepsilon_p)\tilde{\Phi}_p(\tilde{r}_p)d\tilde{r}_p \quad \text{for } \tilde{d}_{\text{sep}}<0 \qquad (11)$$

Note that a "−" sign is introduced in Eq. (11) and the following ones, for using ε_p, as the compressive strain is defined negative in the MP model but positive in the SP model.

Computation of the direct contact pressure $\tilde{P}_d$ requires knowledge on the direct contact area $A_d=1-A_i$, where A_i is the *total influence area* shown in Fig. 2(*c*) for a single particle. The total influence area of the particles as a fraction of total area A_i can be found by the summation of the influence areas of individual particles as follows:

$$A_i = \tilde{\eta}_v \int_0^{\infty} 2\tilde{r}_p \pi \tilde{r}_i^2(-\varepsilon_p)\tilde{\Phi}_p(\tilde{r}_p)d\tilde{r}_p \qquad (12)$$

where $\tilde{r}_i$ is given by Eq. (4). The direct contact area A_d increases as the two surfaces are pushed further into each other in the regime $\tilde{d}_{\text{sep}}<0$ (Fig. 5(*c*)). The direct contact area consists of small areas on the (originally) flat surface, which engage in contact at different levels of compression ε_p. For a given amount of compression ε_p each particle creates a different contact area, which should be added for all the particles to give $A_d(\varepsilon_p)=1-A_i(\varepsilon_p)$, using Eq. (12). Therefore, the direct contact pressure is not uniform and depends on the local compression of each direct contact area. As the compression of the pad is increased, the sections coming into initial contact start to experience low pressure, whereas the sections that have already been in direct contact accumulate more pressure. This cumulative effect is expressed by using the following relationship for the direct contact pressure $\tilde{P}_d$:

$$\tilde{P}_d = \int_{\varepsilon_p^m}^{\varepsilon_p} \tilde{p}_d^{\max}(|\varepsilon_p|-|\varepsilon_p^r|)\frac{dA_d}{d\varepsilon_p^r}d\varepsilon_p^r \qquad (13)$$

Figure 6 shows the typical (calculated) variation of A_d with ε_p, where it can be seen that the direct contact starts at a threshold strain ε_p^m, where $A_d(\varepsilon_p^m)=0$.

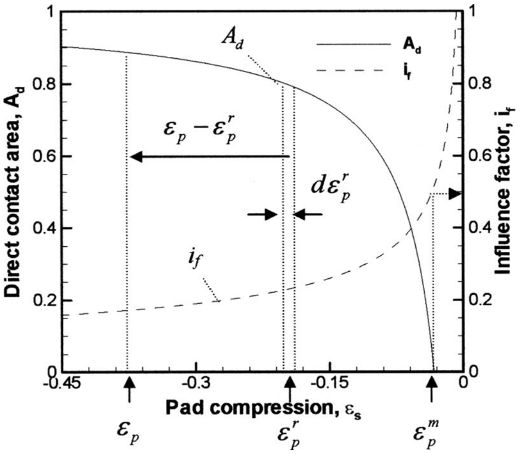

Fig. 6 The variation of direct contact area, A_d, and influence factor, i_f, with pad compression, ε_p.

3.4 Influence Factor. The density of the active particles $\tilde{\eta}_a$ is shown, in Eq. (7), to depend on the particle size $\tilde{r}_p$ and the separation distance $\tilde{d}_{\text{sep}}$. In fact, another factor, which influences this density, is the distribution of the particles in the horizontal plane. Next, the effect of the horizontal interparticle spacing $\tilde{d}_s$ on the density of active particles $\tilde{\eta}_a$ is analyzed. Figure 7(*a*) shows an idealized configuration of seven identical particles, assuming that the particles are evenly spaced at the corners of a hexagon. There are a total of three particles in the hexagon, which has a nondimensional area of $\tilde{A}_h=3\sqrt{3}\tilde{d}_s^{\,2}/2$. In this case, the particle density, $\tilde{\eta}_a$, can be related to the mean spacing between the particles, $\tilde{d}_s$, as

$$\tilde{\eta}_a = \frac{3}{\tilde{A}_h} = \frac{2}{\sqrt{3}\tilde{d}_s^{\,2}} \quad \text{or } \tilde{d}_s = \sqrt{\frac{2}{\sqrt{3}\tilde{\eta}_a}} \qquad (14)$$

For a more generic particle configuration, $\tilde{d}_s$ can be generalized as

$$\tilde{d}_s = \sqrt{\frac{1}{C_p\tilde{\eta}_a}} \qquad (15)$$

where C_p is a constant, which will depend on the relative distances between groups of particles. The mean influence radius of the particles $\tilde{r}_i^{\text{mean}}$ is calculated by

$$\tilde{r}_i^{\text{mean}} = \frac{\tilde{\eta}_v}{\tilde{\eta}_a^m}\int_0^{\infty} 2\tilde{r}_p\tilde{r}_i(-\tilde{\varepsilon}_p)\tilde{\Phi}_p(\tilde{r}_p)d\tilde{r}_p \qquad (16)$$

The influence factor i_f characterizes the overlap of the influence areas between particles and is defined by the following equation:

$$i_f = \frac{\tilde{r}_i^{\text{mean}}}{\tilde{d}_s} \qquad (17)$$

Note that in order for the MP model described in this work to be accurate, the mean influence radius $\tilde{r}_i^{\text{mean}}$ should be greater than $\tilde{d}_s/2$ ($i_f<0.5$) as schematically demonstrated in Figs. 7(*b*)–7(*d*). The particles start to interact when $i_f=0.5$, which corresponds to the separation distance at which direct contact area starts to grow as shown in Fig. 6. As the influence factor i_f becomes larger, the interaction between the particles becomes more significant and the error of the model increases.

3.5 Multiparticle Model Relationships. The effect of particle concentration on the contact conditions in the MP model is investigated next. The relation between the concentrations based on weight η_w and volume $\tilde{\eta}_v$ of the particles is given in Eq. (8). For a slurry with alumina particles, the particle density and the

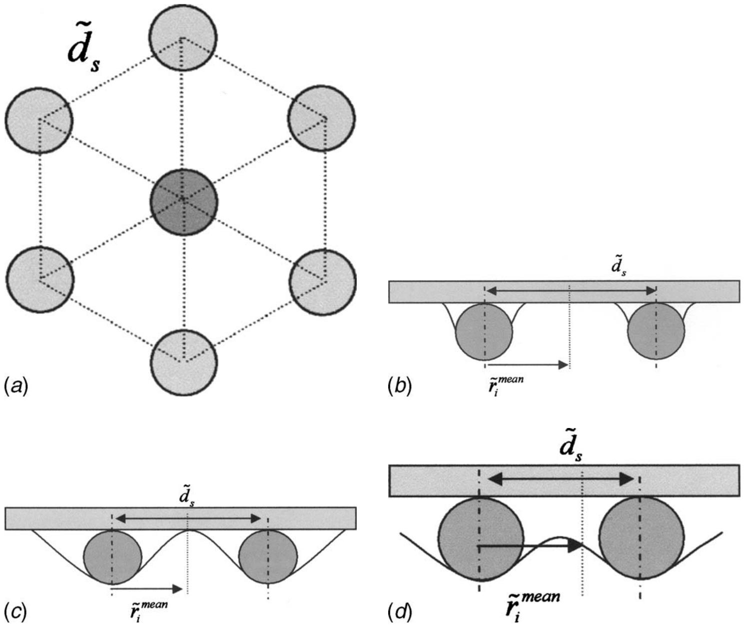

Fig. 7 (*a*) Top view of a particle and its six neighbors. (*b*)–(*d*) Different levels of influence factor i_f.

slurry density are related by $\rho_p/\rho_s=3.7$. The effects of different particle concentrations η_w are investigated in the range $1.25\% < \eta_w < 5\%$ and for mean particle radius of $\tilde{r}_\mu=4$. The PDF for the particle size $\tilde{\Phi}_p$ is assumed to be Gaussian and is given as follows:

$$\tilde{\Phi}_p(\tilde{r}_p)=\frac{1}{\sqrt{2\pi}}e^{-(\tilde{r}_p-\tilde{r}_\mu)^2/2} \tag{18}$$

It should be noted that different PDFs such as the Weibull distribution [7] can easily be implemented into this model.

Figure 8 shows the variation of the mean contact pressure $\tilde{P}_c$ for different separation distances. In the range where $0<\tilde{d}_{\text{sep}}<12$, the load is transferred through the particles and Eqs. (6) and (10) apply. In this range, the mean contact pressure $\tilde{P}_c$ increases rapidly as the separation distance $\tilde{d}_{\text{sep}}$ approaches 0. This figure also demonstrates that for a given separation distance, the mean contact pressure $\tilde{P}_c$ increases with increasing particle concentration η_w. For example, when $\tilde{d}_{\text{sep}}=0$, $\tilde{P}_c$ is found to be 0.005, 0.01, and 0.02 for $\eta_w=1.25\%$, 2.5%, and 5%, respectively.

The mixed contact regime is investigated in the range $-0.45<\varepsilon_p<0$, in Fig. 8, where the mean contact pressure $\tilde{P}_c$ is computed by using Eqs. (6), (11), and (13). In this regime, the number of active particles $\tilde{\eta}_a^m$ remains constant; however, the penetration of each particle increases, and direct contact starts to occur with increasing compression ε_p. Combination of these effects causes the mean contact pressure $\tilde{P}_c$ to increase. At large pad deformation values, $\tilde{P}_c$ depends predominantly on direct wafer-to-pad contact. On the other hand, when the separation distance is near zero, a transition region exists where only particle contacts support the surfaces even though $\tilde{d}_{\text{sep}}<0$. The fraction of mean particle con-

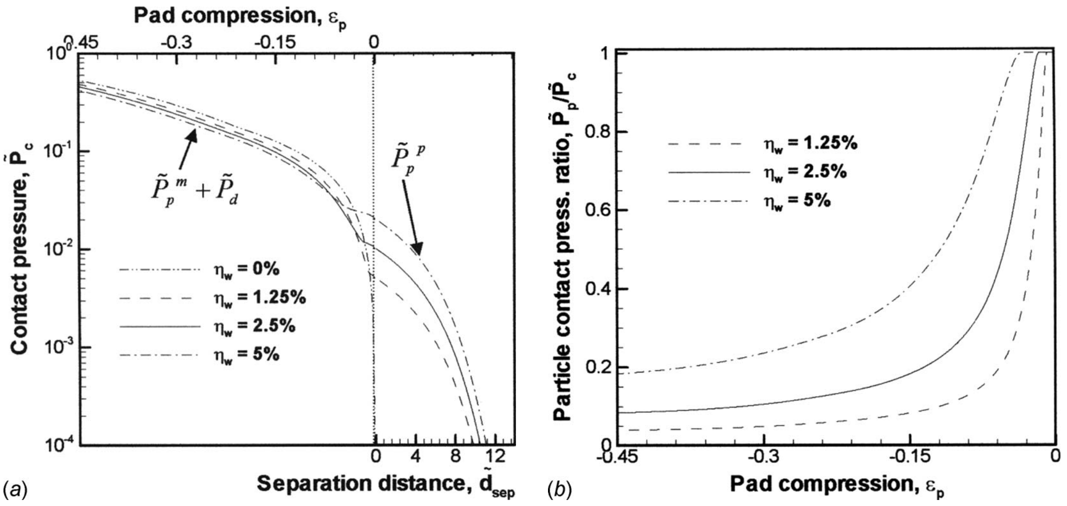

Fig. 8 (*a*) The contact pressure $\tilde{P}_c$ in pure particle ($\tilde{P}_p^p$) and mixed ($\tilde{P}_p^m+\tilde{P}_d$) contact regimes for different particle concentrations, η_w=1.25%, 2.5%, and 5%, and (*b*) particle contact pressure ratio $\tilde{P}_p^m/\tilde{P}_c$

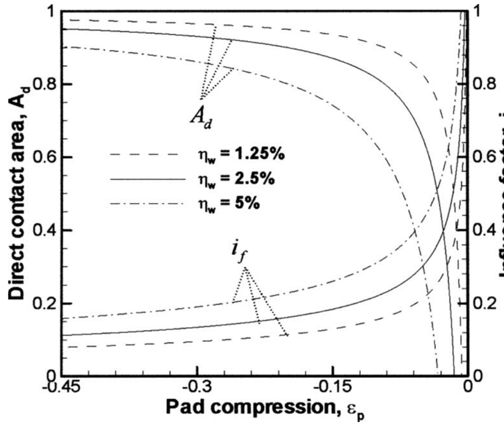

Fig. 9 The direct contact area, A_d, and influence factor, i_f, in mixed contact regime for different particle concentrations, η_w =1.25%, 2.5%, and 5%

tact pressure to the total contact pressure, $\tilde{P}_p^m/\tilde{P}_c$, as a function of the pad compression ε_p is shown in Fig. 8(*b*). This figure shows that in the mixed contact regime, as the amount of compression increases the fraction of the force carried by the particle contacts decreases. This figure also shows that direct contact does not occur until a critical value ε_p^m is reached. The *transition region* is, therefore, defined as $\varepsilon_p^m < \varepsilon_p < 0$. In the transition region, the mean contact pressure is nearly constant, as contact is entirely enabled by the particles. Beyond the transition region the mean contact pressure, $\tilde{P}_c$, (Fig. 8(*b*)) increases linearly with pad compression, $\tilde{\varepsilon}_p$, much like in Eq. (5). The critical ε_p^m values are approximately −0.007, −0.015, and −0.033 for particle concentrations, η_w=1.25%, 2.5%, and 5%, respectively. At high particle concentrations η_w, the fact that there are more particles in the interface retards the formation of direct contacts and allows particle contacts to support the load for deeper penetrations.

Figure 9 shows the direct contact area A_d (=$1-A_i$) computed from Eq. (12) and the influence factor i_f computed by using Eq. (17). It is seen that direct contact area A_d is zero in the transition region. As the pad is compressed further ($\varepsilon_p \to -0.45$) mixed contact is established; the direct contact area A_d increases rapidly with ε_p, gradually leveling off. Note that it appears that A_d will level off to a value less than 1, as part of the contact area is composed of spherical particles with influence contact area A_i. This figure also shows that for the particle concentrations chosen here, influence factor $i_f < 0.5$ in the mixed contact regime indicating that the influence areas of the particles are well separated.

4 Single Asperity Model

Next, in the SA model where contact of a spherical asperity with a flat deformable surface is analyzed with rigid spherical particles are entrapped in the asperity-flat-surface interface, as shown in Fig. 1(*b*). While the asperity is made of a hyperelastic solid it actually endures small deformations, which are in the linear range of the material behavior, as shown in Eq. (5) and Fig. 4. Therefore, no generality is lost when the bulk deformation behavior of the system is represented by modeling the asperity as a rigid sphere and the flat surface as the deformable medium [14]. A schematic description of the SA interface, shown in Fig. 10, assumes that the sphere can be approximated as a parabola near the contact region. Therefore, the local separation $\tilde{u}$ along the radial direction $\tilde{\rho}$ can be approximated as $\tilde{u}=\tilde{u}_0+\tilde{\rho}^2/2\tilde{R}_b$, where $\tilde{u}_0$ is the separation distance at the center of contact and $\tilde{R}_b$ is the bulk radius of the asperity. Considering the elastic deformation of the deformable medium $\tilde{w}_b$, the relationship for the local separation is expressed as [14]

$$\tilde{u} = \tilde{u}_0 + \frac{\tilde{\rho}^2}{2\tilde{R}_b} + \tilde{w}_b \tag{19}$$

The diameter of a pad asperity is three orders of magnitude larger than the mean particle diameter, and the number of particles entrapped under the deformed asperity is shown to be more than 100 as demonstrated later in Sec. 4.1.1. This situation is very similar to the elastic contact of rough spheres analyzed by Greenwood and Tripp [14]. In this work, the effect of the particles trapped in the interface is represented by introducing a "contact-layer" (Fig. 10) whose deformation behavior has just been introduced in the MP model in Sec. 3. This layer transfers the forces between the two surfaces.

The circular contact interface is divided into annular areas as shown in Fig. 10. Each annular area is bound by the inner radius, $\tilde{\rho}_i$, and the outer radius, $\tilde{\rho}_{i+1}$. The annular areas interact with each other through the bulk deformation of the surface $\tilde{w}_{b_i}$. An axisymmetric FE model of the deformable medium is constructed to obtain the bulk deformation, $\tilde{w}_{b_i}$, induced by the local contact pressure, $\tilde{p}_i$, acting in each annular region. The bulk deformation $\tilde{w}_{b_i}$ is determined by averaging the vertical deflection of the nodes located at $\tilde{\rho}_i$ and $\tilde{\rho}_{i+1}$ in the finite element model. The bulk deformation, $\tilde{w}_{b_i}$, is used to calculate the local separation, $\tilde{u}_i$, which is then substituted into the multiparticle model (Eqs. (10)–(13)) to obtain the local contact pressure, $\tilde{p}_i$. The equilibrium local contact pressure, $\tilde{p}_i$, is iteratively found by repeating these steps until the total contact force, $\tilde{F}_c^s$, converges.

The local contact pressure, $\tilde{p}_i$, is found by using the MP model (Eq. (6)) for a given local separation, $\tilde{u}_i$. Note that the particle contact force $\tilde{P}_p^p$ depends on the local separation $\tilde{u}$ (=$\tilde{d}_{\text{sep}}$), whereas the mixed contact force $\tilde{P}_p^m+\tilde{P}_d$ is a function of the average compressive strain ε_p, and thus depends on the layer thickness $\tilde{t}_s$. Therefore, a thickness value is required for the contact-layer, particularly where $\tilde{u}_i<0$. The contact-layer thickness is chosen by searching for the value of $\tilde{t}_s$ that minimizes the error between computed results and the Hertz contact by neglecting the effect of particles (η_w=0). Figure 11 shows the deviation of the

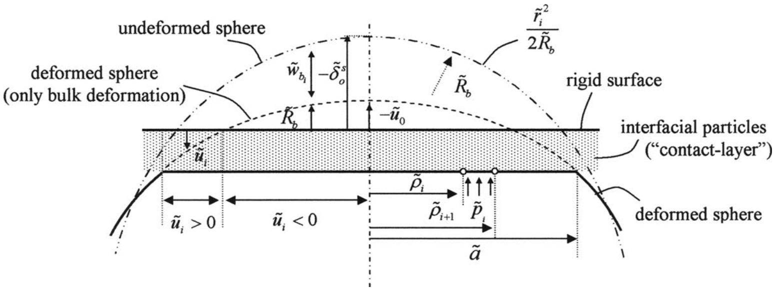

Fig. 10 Single asperity model

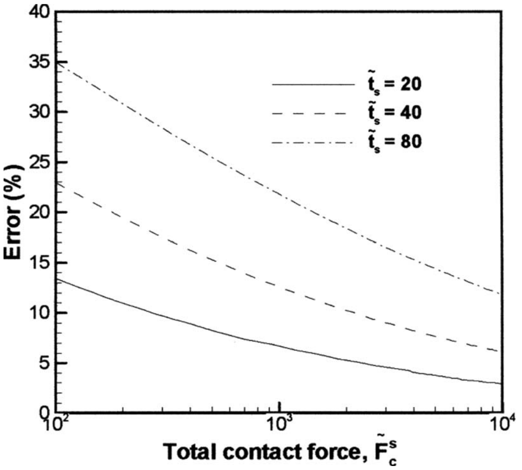

Fig. 11 The error between the predicted maximum contact pressure with respect to the Hertz model ($\tilde{p}_0 = (3\tilde{F}_c^s/(2\pi^3\tilde{R}_b^2))^{1/3}$) utilizing different layer thicknesses $\tilde{t}_s$

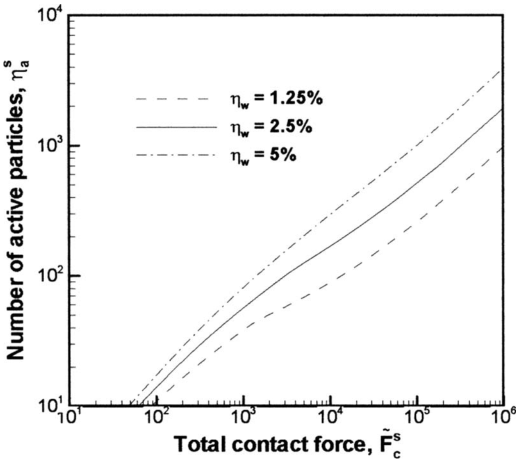

Fig. 12 The number of active particles, n_a^s, as a function of the total contact force, $\tilde{F}_c^s$, for different particle concentrations, η_w

computed maximum contact pressure $\tilde{p}_0$ with respect to the Hertz contact model $\tilde{p}_0=(3\tilde{F}_c^s/(2\pi^3\tilde{R}_b^2))^{1/3}$ for different values of the layer thickness $\tilde{t}_s$. As expected, thinner layers give better predictions to Hertz contact, as in that case the compressive strain ε_p becomes large for a given separation $\tilde{u}$. However, the computation times increase for thinner layers. It is, in fact, seen that, in the mixed contact region, the contact-layer acts as a penalty parameter, used commonly in imposing contact conditions in FE analysis, but preserves the particle contact behavior in the particle contact region of the SA interface. Based on the accuracy of the solution and the computation time, the layer thickness $\tilde{t}_s=20$ is used in this study.

The deformable medium is discretized with 4700 four-noded axisymmetric elements (PLANE182). The mesh of the deformable medium is finer near the contact zone; in particular, the element size is adjusted to be smaller near the outside edge of the contact region, in order to compute the contact radius $\tilde{a}$ accurately. Only the bottom nodes of the deformable medium are constrained in the direction of the bulk deformation and all other boundaries are left free. The thickness and the outer radius of the deformable medium are taken as $7\tilde{a}$ and $8.5\tilde{a}$. These values are found by trial and error to be sufficiently large so that the results are not influenced by the remote boundary effects even for the largest applied loads.

The parameters of this model, which are nondimensionalized as shown in Table 1, are the mean particle size, $\tilde{r}_\mu$, particle concentration, η_w, and bulk radius of the asperity, $\tilde{R}_b$. The direct contact pressure, $\tilde{p}_d$, the particle contact pressure, $\tilde{p}_p$, the variation of the direct contact area in the contact zone, A_d, the total contact force, $\tilde{F}_c^s$, the total particle contact force, $\tilde{F}_p^s$, the total direct contact area, A_d^s, and the contact radius, $\tilde{a}$, are calculated for a given separation distance at the center of contact, $\tilde{u}_0$. The numerical algorithm consisting of two main iteration steps to implement the outlined solution approach is explained in the Appendix.

4.1 Results of Single Asperity Model. The same slurry properties described in the MP model, typical for CMP-slurry containing alumina abrasives, are used to evaluate the results of the SA model. In practice, the mean diameter of abrasive particles $2r_\mu$ are typically in the range 25–100 nm, and the pad asperity radius R_b is on the order of 50 μm. The nondimensional values are chosen to reflect these ranges. The effect of the asperity radius is studied in the range $4000<\tilde{R}_b<16{,}000$, while taking the particle concentration $\eta_w=2.5\%$. The effect of the particle concentration is studied in the range $1.25\% \leqslant \eta_w \leqslant 5\%$, while $\tilde{R}_b$ is 8000. The separation distance at the center of contact, $\tilde{u}_0$, is increased with increments of $\tilde{u}_{\text{inc}}=0.02$. The initial value of the relaxation factor r_f is 0.8 and gradually decreased to 0.025 as the penetration is increased in order to achieve convergence, as described in the Appendix.

In order to obtain an estimate for the contact force $\tilde{F}_c^s$ on a pad asperity the GW model can be used. The mean contact pressure, P_c, and the number of asperities in contact per unit area, n_{asp}, can be found by using Eq. (9). The nondimensional mean contact force on each asperity can then be determined as $(\tilde{F}_c^s)_{\text{mean}} = (P_c/n_{\text{asp}})((1-\nu_s^2)/E_s\sigma_p^2)$. The typical CMP pad has elastic modulus $E_s=10-100$ MPa, asperity peak standard deviation ~ 5 μm, asperity density $\eta \sim 2\times 10^8/\text{m}^2$, and asperity radius $R_b \sim 50$ μm. The applied pressure in CMP varies between $P_c \sim 10$ kPa and 100 kPa. The standard deviation of the abrasive particle size distribution can be taken as $\sigma_p \sim 6.25$ nm considering the mean particle radius of $r_p \sim 25$ nm. Evaluating the relations given in Eq. (9) for these values shows that the mean contact force on the asperities $(\tilde{F}_c^s)_{\text{mean}}$ varies in the range $2\times 10^5<(\tilde{F}_c^s)_{\text{mean}}<4\times 10^5$, while the applied pressure is increased from 10 kPa to 100 kPa for $E_s=100$ MPa, and in the range $3\times 10^5<(\tilde{F}_c^s)_{\text{mean}}<9\times 10^5$ for $E_s=10$ MPa. In this work the effect of the contact force $\tilde{F}_c^s$ is investigated in the range 10^2-10^6, considering the variability in size of the particles and the contact conditions.

4.1.1 Effect of Particles on Contact Interface. In the MP model, it is shown that the contribution of the particle contacts to the overall force balance depends on the number of active particles in contact with each asperity η_a. The SA model implicitly assumes that large numbers of particles are present at each asperity contact interface, so that the statistical definition of the particle size distribution and the averaging of the particle effects used in the model are justified. Therefore, it is important to evaluate the number of active particles n_a^s in the asperity's contact interface. This variable is computed by summing the number of particles trapped in each annular area in the SA model by using the relationship $n_a^s=\Sigma_i^N \pi(\tilde{\rho}_{i+1}^2-\tilde{\rho}_i^2)\tilde{\eta}_{ai}$, where the nondimensionalized concentration of active particles $\tilde{\eta}_{ai}$ for each annular region is computed by using Eq. (7) with the lower limit of the integral as the $\tilde{u}_i$ value used in Eq. (19). Note that the particle contact force and direct contact area are computed similarly, by using Eqs. (6) and (12), respectively. Figure 12 shows that the number of active particles n_a^s in the single asperity interface increases with particle

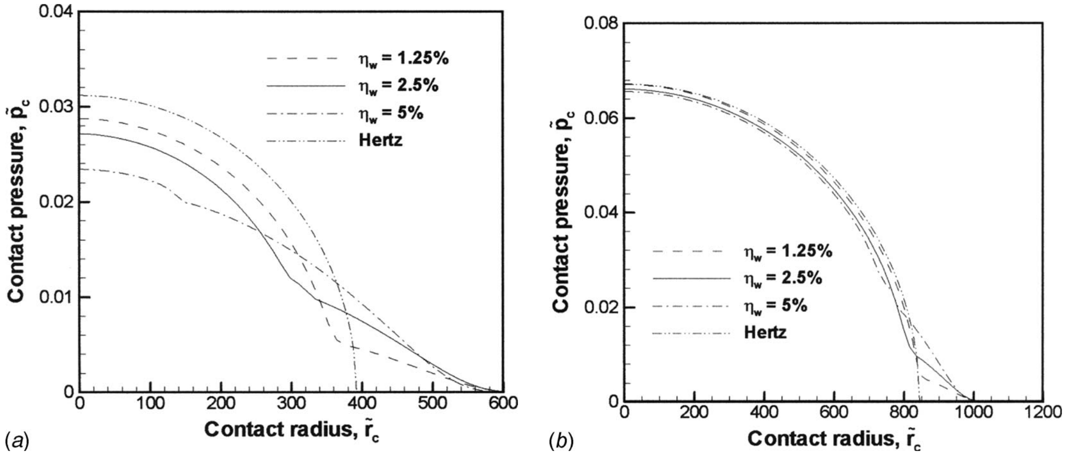

Fig. 13 The effect of the particle concentration, η_w, on the contact pressure, $\tilde{p}_c$, distribution in the contact interface for contact force values of (*a*) $\tilde{F}_c^s=10^4$ and (*b*) $\tilde{F}_c^s=10^5$

concentration η_w and the total applied force $\tilde{F}_c^s$ as expected. It should be noted that n_a^s remains greater than 100 for all η_w studied and when the total contact force $\tilde{F}_c^s > 10^4$.

The computed contact pressure $\tilde{p}_c$ distribution in the asperity contact interface is plotted in Fig. 13, for two different values of the total contact force, $\tilde{F}_c^s=10^4$ and 10^5. Figure 13(*a*) shows that the presence of the rigid particles in the interface causes a significant deviation of the contact pressure distribution from the Hertz contact, when the total force is low $\tilde{F}_c^s=10^4$. Particle concentration η_w has an important effect on this distribution, causing more deviation at higher η_w values. Figure 13(*a*) also shows that the contact area is predicted to be larger than that of the Hertz contact when particles are involved in contact. In fact, this effect causes a reduction in the maximum contact pressure at the center of contact, $\tilde{p}_0$. On the other hand, when the contact force $\tilde{F}_c^s=10^5$, the contact pressure distribution for different particle concentrations and Hertz contact become almost identical. This result stems from the fact that the local penetration in the contact zone is so large that direct contacts dominate the contact interface and the relative effects of particle contacts, which are limited to the outside edge of the contact zone, becomes small. These figures show that higher elastic modulus (E_s) and larger particle standard deviation (σ_p) cause larger deviations from the Hertz contact, considering the deviation from Hertz contact is more significant at lower values of the total contact force ($\tilde{F}_c^s=F_c^s(1-\nu_s^2)/E_s\sigma_p^2$).

It is apparent from Fig. 13 that the contact interface can be divided into three different regions, based on the effects of direct and particle contact. In fact, the presence of these regions can be explained better in Fig. 14, where the fraction of particle contact pressure to total contact pressure, $\tilde{p}_p/\tilde{p}_c$, and the direct contact area A_d in the interface are plotted. This figure shows that, at the outside edge of the contact region, where $\tilde{p}_p/\tilde{p}_c=1$, pure particle contact is the responsible mechanism for the contact pressure. On the other hand, direct contact is the dominant mechanism near the center of contact, where $\tilde{p}_p/\tilde{p}_c<1$, as the particles become embedded in the elastic surface, causing an increase in the direct contact area. There is a transition region between direct contact and particle contact dominant regions in which the effects of particle and direct contact are comparable. The direct contact area A_d is initially 0 at the outside edge of the contact zone. Toward the center of the contact, the deformation of the asperity increases, which in turn causes a larger area to come into direct contact. Of course the presence of the particles delays the occurrence of the direct contact, and as expected for higher particle concentration, η_w direct contact covers a smaller area.

4.1.2 Effect of Total Contact Force. The above results show that the total contact force $\tilde{F}_c^s$ acting on the asperity could have a significant influence on the behavior of the contact interface. It is

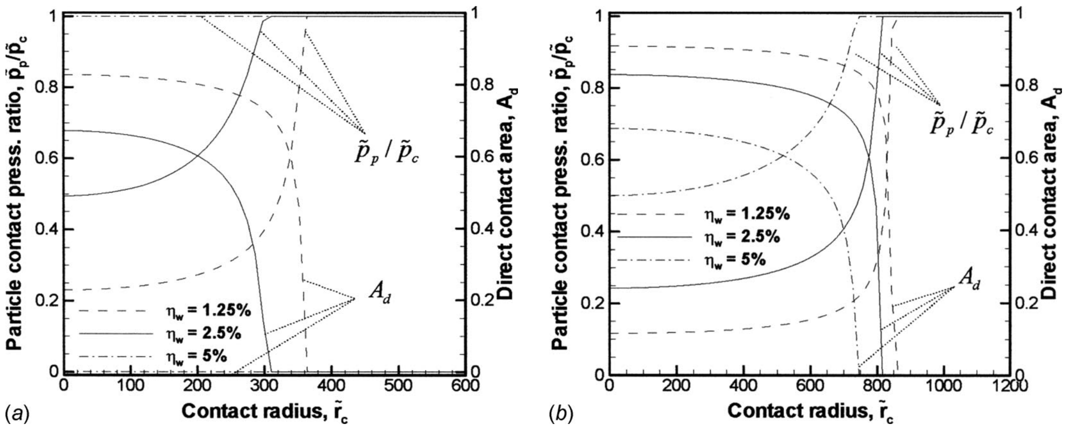

Fig. 14 The effects of the particle concentration, η_w, on the distribution of ratio of the particle contact pressure to the total contact pressure, $\tilde{p}_p/\tilde{p}_c$, and the direct contact area, A_d, in the contact zone for contact force values of (*a*) $\tilde{F}_c^s=10^4$ and (*b*) $\tilde{F}_c^s=10^5$

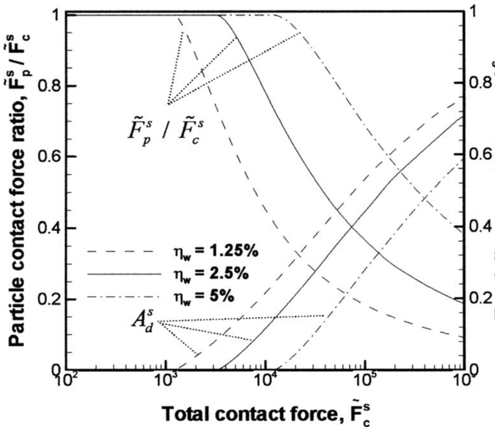

Fig. 15 The variation of the particle contact force as a fraction of the total contact force, $\tilde{F}_p^s/\tilde{F}_c^s$, and the direct contact area, A_d^s, with the total contact force, $\tilde{F}_c^s$, for different particle concentrations, η_w

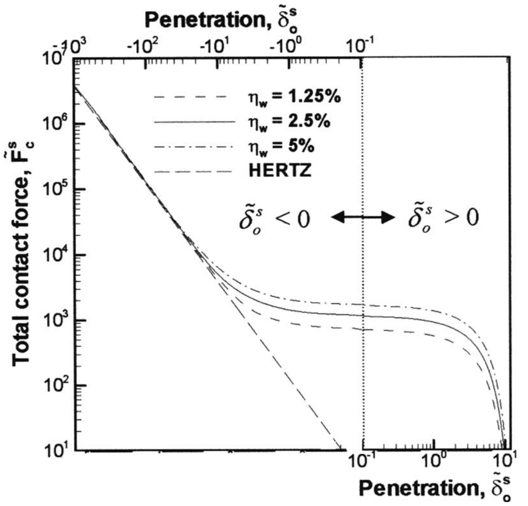

Fig. 16 The variation of the total contact force, $\tilde{F}_c^s$, with the penetration at the center of contact, $\tilde{\delta}_0^s$, for different particle concentrations η_w

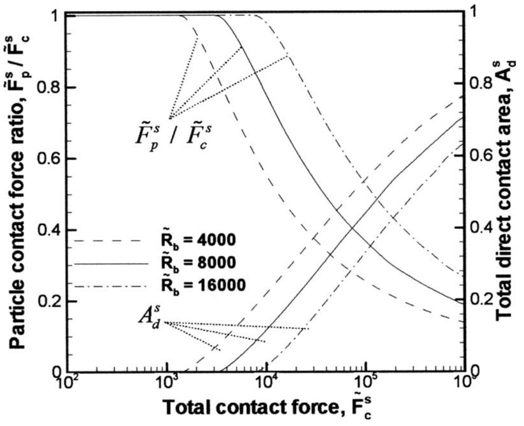

Fig. 18 The variation of the particle contact force as a fraction of the total contact force, $\tilde{F}_p^s/\tilde{F}_c^s$, and the direct contact area, A_d^s, with the total contact force, $\tilde{F}_c^s$, for different asperity radii, $\tilde{R}_b$

therefore important to investigate the effect of $\tilde{F}_c^s$. Figure 15 shows the variation of the fraction of total force carried by the particles, $\tilde{F}_p^s/\tilde{F}_c^s$, and the total direct contact area, A_d^s, as a function of the total contact force, $\tilde{F}_c^s$, for the three different particle concentrations, η_w. This figure shows that for low $\tilde{F}_c^s$ values the entire load is carried by the particles ($\tilde{F}_p^s/\tilde{F}_c^s=1$). When the direct contact starts to become significant at higher loads, this ratio gradually becomes lower than 1. As expected, the direct contact starts to become more significant for lower values of the particle concentrations. Following a similar trend, the total contact area increases with increasing $\tilde{F}_c^s$ values.

4.1.3 Effect of Penetration Depth. According to Hertz contact model the total contact force is expected to vary with the 3/2 power of the penetration at the center of contact ($\tilde{\delta}_0^s$). The presence of the particles in the contact interface is expected to modify this relation. In this work, the negative values of the penetration are assumed to cause contact of the idealized asperity as shown in Fig. 10. However, the particles trapped in the interface cause contact even when $\tilde{\delta}_0^s>0$. The effect of penetration ($\tilde{\delta}_0^s$) is plotted in Fig. 16. As expected the model predicts that the particles trapped between the surfaces become engaged in contact, causing the total contact force $\tilde{F}_c^s$ to become nonzero when $\tilde{\delta}_0^s>0$, while the Hertz

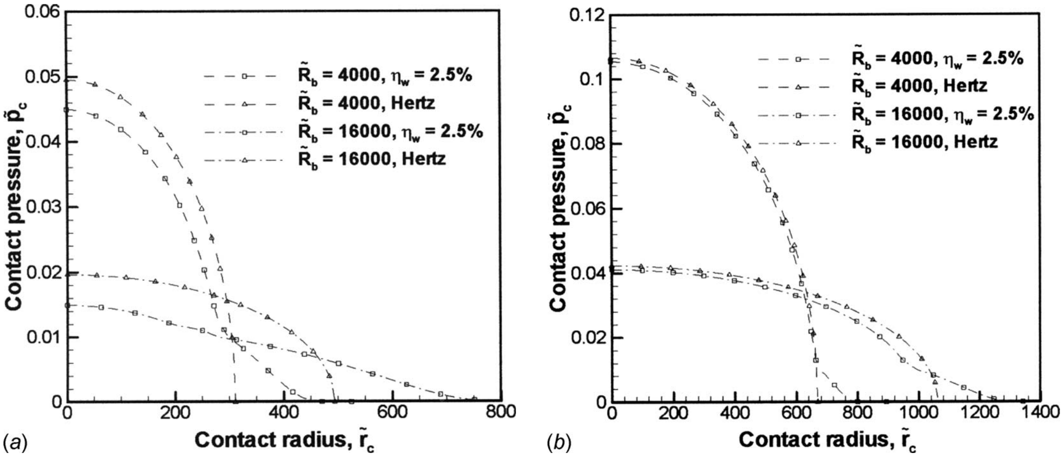

(*a*) (*b*)

Fig. 17 The effect of the asperity radius, $\tilde{R}_b$, on the contact pressure, $\tilde{p}_c$, distribution along the contact zone, for contact force values of (*a*) $\tilde{F}_c^s=10^4$ and (*b*) $\tilde{F}_c^s=10^5$

contact model clearly predicts zero contact force. In this range, the total contact force $\widetilde{F}_c^s$ increases with η_w for the same amount of penetration, as more particles are present when particle concentration is high. Figure 16 also shows what happens when the penetration is increased or $\widetilde{\delta}_0^s$ becomes negative. The total contact force $\widetilde{F}_c^s$ estimated by Hertz contact is smaller than the particle model for small penetration values. However, as the penetration is increased further, the variation of the total contact force, $\widetilde{F}_c^s$, with the penetration, $\widetilde{\delta}_0^s$, becomes similar to Hertz contact. This result is in agreement with the contact pressure distribution that is shown to be similar at high total contact force, $\widetilde{F}_c^s$, in Fig. 13. It is also noted that the effect of particle concentration diminishes at large penetration depths.

4.1.4 Effect of Asperity Radius. The effect of asperity radius $\widetilde{R}_b$ is presented in Figs. 17 and 18. The computed contact pressure $\widetilde{p}_c$ variations in the contact interface of the asperity are plotted in Figs. 17(*a*) and 17(*b*) for $\widetilde{F}_c^s=10^4$ and 10^5, respectively. These figures show that, for a given total force, the predicted contact pressure distribution when abrasive particles are in the interface deviates more with respect to the Hertz contact, when the asperity radius increases.

The total direct contact area, A_d^s, and the ratio of particle contact force to total contact force, $\widetilde{F}_p^s/\widetilde{F}_c^s$, are plotted in Fig. 18, as a function of the total contact force, $\widetilde{F}_c^s$, for different asperity radii, $\widetilde{R}_b$. The contact force required to initiate the direct contact becomes smaller, as the asperity radius is decreased. The direct contact area, A_d^s, for smallest asperity radius, $\widetilde{R}_b=4000$, remains to be larger in the whole range of total contact force studied. Moreover, the particle contact force ratio F_p^s/F_c^s is higher for the asperities with a larger radius. These results are attributed to the fact that for a given total force, a larger contact area but lower contact pressure is predicted when the asperity radius increases. In fact, this is even evidenced by the Hertz relations for the contact radius $\widetilde{a}=(3\widetilde{F}_c^s\widetilde{R}_b/2)^{1/3}$ and maximum pressure $\widetilde{p}_0=(3\widetilde{F}_c^s/(2\pi^3\widetilde{R}_b^2))^{1/3}$. As the contact pressure is lower on a larger asperity, the particles will have a lower tendency to penetrate into the elastic solid and thus they will carry a larger proportion of the load.

5 Summary and Conclusions

The single asperity model developed in this paper can be used to characterize the contact of a single asperity with a rigid flat surface, when rigid spherical particles are present in the contact interface. The external load on the asperity is transferred to the rigid surface by the particles and by the direct contact of the elastic pad to rigid surface. The degree to which the particles become embedded into the deformable material affects the interfacial contact conditions.

This work showed that one of the effects of the particles on the overall contact behavior is to distribute the contact over a larger area. Consequently, the maximum contact pressure at the center of contact decreases with respect to the prediction of the Hertz theory. This work also showed that the particles will have a lower tendency to penetrate into the elastic solid, when they are caught in the interface of a relatively large asperity. For a given total contact force, this means that an increased proportion of the total contact force will be carried by the particles if the asperity radius is increased.

The particle contact force is an important output of the model as it can be used to determine the material removal rate in CMP. The results show that the total contact force is carried by the particle contacts at small loads in the pure particle contact regime. In fact, the contact force could be nonzero even when the surfaces are separated from each other. For high loads, the fraction of the total load carried by particle contacts starts to decrease rapidly as the contact pressure develops at the direct contact interface at a higher rate than the rate of increase in the particle contact interface. This implies that increasing the total contact force may *not* necessarily translate to a significant increase in the particle contact force. This finding can be used to shed light onto different experimental trends of the material removal rate (MRR) variation with applied pressure for hard and soft CMP pads [15]. The MRR is experimentally found to increase linearly with applied pressure for hard pads, whereas it depends sublinearly on the applied pressure for soft pads. Based on this work, the occurrence of the direct contact for the soft pads can be considered as the reason for this sublinear dependence.

At high particle concentrations the influence area of the particles starts to overlap as the mean distance between the particles decreases. This slows down the occurrence of direct contact for a given load. Therefore, high particle concentration provides a *more favorable* condition to effectively transfer the applied force through the particles. The CMP studies [15,16] investigating the influence of the particle concentration on the MRR show that the MRR increases linearly with particle concentration when the particle concentration is low, which is confirmed by the single asperity model showing larger particle contact force for higher particle concentration. These experimental studies also show that the MRR levels off at high particle concentration. This finding is in contrast with the prediction of the SA model showing a continuous increase in the particle contact force with higher particle concentration. However, the single model developed here is by itself insufficient to model a multi-asperity contact situation where the pad's roughness and porous structure, the dynamics of the particles (sliding versus rolling), and the hardness of the passivated layer are at play. The implementation of the single asperity model developed here into a multi-asperity contact and wear model is the subject of the ongoing research.

Acknowledgment

Partial support of S.M. for this work was provided by the National Science Foundation (Award No. NSF-0425826). Part of this work was carried out by S.M. at the Civil and Environmental Engineering Department of the Massachusetts Institute of Technology during a sabbatical leave.

Appendix: Numerical Algorithm for the Solution of the Single Asperity Model

In the first step controlled by the inner loop (Fig. 19), the rigid part of the separation distance, $\widetilde{u}_i^r$, is fixed and the variable part, $\widetilde{u}_i^v$, is updated using the bulk deformation from the finite element solution as

$$\widetilde{u}_i=\widetilde{u}_i^{\,r}+\widetilde{u}_i^{\,v} \tag{A1}$$

where $\widetilde{u}_i^r$ and $\widetilde{u}_i^v$ for the *k*th iterative step of the inner loop are given as

$$(\widetilde{u}_i^{\,r})^k=\widetilde{u}_0+\frac{\widetilde{\rho}_i^{\,2}}{2\widetilde{R}_b}+(1-r_f)(\widetilde{w}_{b_i}^0-\widetilde{w}_{b_0}^0) \tag{A2}$$

$$(\widetilde{u}_i^{\,v})^k=r_f(\widetilde{w}_{b_i}^k-\widetilde{w}_0^k) \tag{A3}$$

The updated separation distance, $\widetilde{u}_i$, is substituted into the multiparticle model to find the local contact pressure, $\widetilde{p}_i$, acting in each annular region (Eqs. (10)–(13)). The local contact pressure, $\widetilde{p}_i$, is then applied on the contact elements of the finite element model, which is solved to obtain the bulk deformation, $\widetilde{w}_{b_i}$. The separation distance, $\widetilde{u}_i$, is calculated from the updated bulk deformation, $\widetilde{w}_{b_i}$ using Eqs. (A1)–(A3). The local contact pressure, $\widetilde{p}_i$, on the contact elements is integrated to find the total contact force, $\widetilde{F}_c^s$. The inner loop ends as the variation of $\widetilde{F}_c^s$ between successive

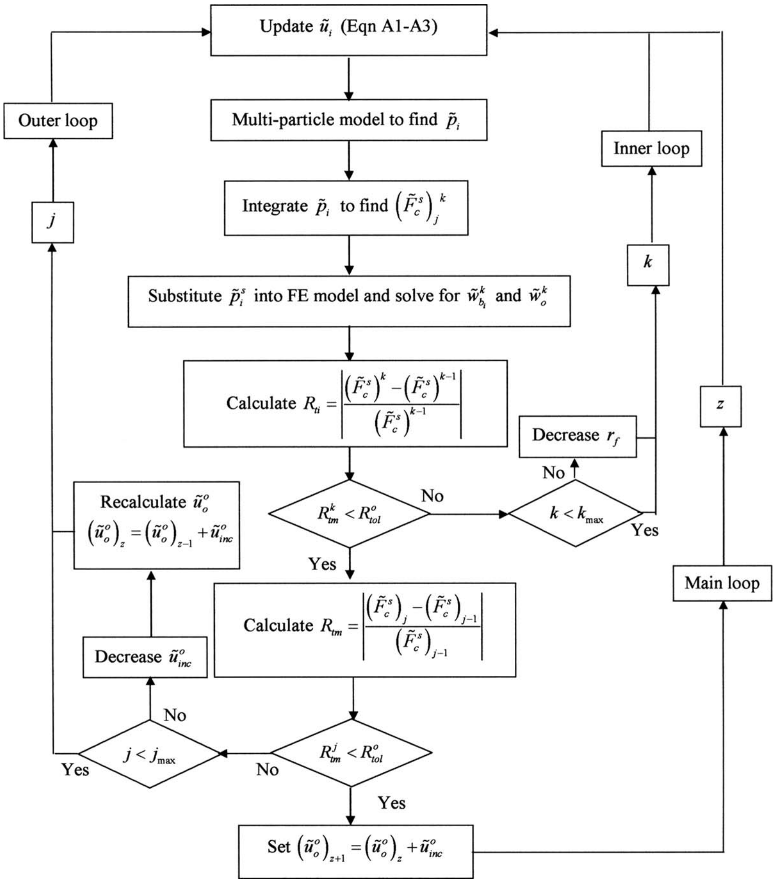

Fig. 19 Numerical algorithm for the solution of the single asperity model

iterations is smaller than the convergence tolerance for the inner loop.

If the solution does not converge as the number of iterations for the inner loop, k, exceeds the maximum number of iterations, $k_{\max}$ ($k > k_{\max}$), the separation distance, $\tilde{u}_i$, is recalculated with a smaller relaxation factor, r_f, in Eqs. (A2) and (A3) so that the rigid part of the separation distance, $\tilde{u}_i^r$, becomes larger to enhance the convergence behavior. Once convergence is obtained for the inner loop, $\tilde{u}_i^r$ is updated for the next iteration $(j+1)$ of the outer loop by using $\tilde{u}_i^r$ from the converged solution of $(j-1)$th and jth steps as

$$(\tilde{u}_i^r)_{j+1} = (1 - r_f)(\tilde{u}_i^r)_{j-1} + r_f(\tilde{u}_i^r)_j \tag{A4}$$

The outer loop controls the convergence behavior of the total contact force $\tilde{F}_c^s$ obtained from the inner loop. If the successive values of $\tilde{F}_c^s$ from converged solution of the inner loop varies within the convergence tolerance, the bulk deformation is assumed to be in equilibrium with the contact pressure for the given separation distance at the center of contact, $\tilde{u}_0$. Once the solution is obtained for the direct contact pressure $\tilde{p}_d$, particle contact pressure $\tilde{p}_p$, and contact radius $\tilde{a}$ using the converged bulk deformation $\tilde{w}_b$, the separation distance at the center of contact, $\tilde{u}_0$, is increased with an increment, $\tilde{u}_{\text{inc}}$.

The initial guess for the bulk deformation $\tilde{w}_{b_i}$ of the current step is taken from the converged solution of previous step. If convergence criteria cannot be satisfied in the outer loop before the number of iterations for the outer loop, j becomes large $(j > j_{\max})$, the increment $\tilde{u}_{\text{inc}}$ is decreased, and the outer loop is restarted with the new separation distance at the center of contact $\tilde{u}_0$ in the main loop. In the first step, the total contact force, $\tilde{F}_c^s$, is small enough to ensure convergence even when the initial guess for the bulk deformation, $\tilde{w}_{b_i}$, is taken to be 0.

The convergence rate is high for small contact force (small penetration depth) even when the initial guess for the bulk deformation $\tilde{w}_{b_i}$ is taken to be 0. However, as the penetration depth is increased, the convergence behavior rapidly changes. The convergence for large penetration depths is achieved by improving the initial guess for the bulk deformation $\tilde{w}_{b_i}$. The initial guess for the bulk deformation $\tilde{w}_{b_i}$ of each iteration is obtained from the previous iteration. This approach improves the convergence behavior; however, convergence problems can still be encountered when the penetration depth is further increased. In order to enhance the convergence behavior, the rigid part of the separation distance is not assumed to be spherical but the new shape is interpolated considering the bulk deformation $\tilde{w}_{b_i}$ from the previous iteration. A relaxation factor, r_f, which is defined as the fraction of the bulk deformation, $\tilde{w}_{b_i}$ that is used for the variable part of the separation distance is utilized. The relaxation factor r_f is reduced at large penetration depths to achieve convergence, with the cost of increased computation times.

References

[1] Oliver, M. R., 2004, *Chemical Mechanical Planarization of Semiconductor Materials*, Springer, New York.

[2] Levert, J. A., Danyluk, S., and Tichy, J., 2000, "Mechanism for Subambient Interfacial Pressures While Polishing With Liquids," ASME J. Tribol., **122**(2), pp. 450–457.

[3] Qin, K., Moudgil, B., and Park, C. W., 2004, "A Chemical Mechanical Polishing Model Iincorporating Both the Chemical and Mechanical Effects," Thin Solid Films, **446**(2), pp. 277–286.

[4] Bastawros, A., Chandra, A., Guo, Y., and Yan, B., 2002, "Pad Effects on Material-Removal Rate in Chemical-Mechanical Planarization," J. Electron. Mater., **31**(10), pp. 1022–1031.

[5] Zhao, Y., and Chang, L., 2002, "A Micro-Contact and Wear Model for Chemical-Mechanical Polishing of Silicon Wafers," Wear, **252**(3–4), pp. 220–226.

[6] Greenwood, J. A., and Williamson, J. B. P., 1966, "Contact of Nominally Flat Surfaces," Proc. R. Soc. London, Ser. A, **295**, pp. 300–319.

[7] McCool, J. I., 2000, "Extending the Capability of the Greenwood Williamson Microcontact Model," ASME J. Tribol., **122**(3), pp. 496–502.

[8] Johnson, K. L., 1985, *Contact Mechanics*, Cambridge University Press, Cambridge.

[9] Zhang, F., Busnaina, A. A., and Ahmadi, G., 1999, "Particle Adhesion and Removal in Chemical Mechanical Polishing and Post-CMP Cleaning," J. Electrochem. Soc., **146**(7), pp. 2665–2669.

[10] Luo, J., and Dornfeld, D. A., 2001, "Material Removal Mechanism in Chemical Mechanical Polishing: Theory and Modeling," IEEE Trans. Semicond. Manuf., **14**, pp. 112–133.

[11] Castillo-Mejia, D., Kelchner, J., and Beaudoin, S., 2004, "Polishing Pad Surface Morphology and Chemical Mechanical Planarization," J. Electrochem. Soc., **151**(20), pp. 271–278.

[12] Wu, H. C., 2004, *Continuum Mechanics and Plasticity*, Chapman and Hall, London/CRC, Boca Raton, FL.

[13] Kim, A. T., Seok, J., Tichy, J. A., and Cale, T. S., 2003, "A Multiscale Elastohydrodynamic Contact Model for CMP," J. Electrochem. Soc., **150**(9), pp. 570–576.

[14] Greenwood, J. A., and Tripp, J. H., 1967, "The Elastic Contact of Rough Spheres," ASME J. Appl. Mech., **34**, pp. 153–160.

[15] Guo, L., and Subramanian, R. S., 2004, "Mechanical Removal in CMP of Copper Using Alumina Abrasives," J. Electrochem. Soc., **151**(2), pp. 104–108.

[16] Bielmann, M., Mahajan, U., and Singh, R. K., 1999, "Effect of Particle Size During Tungsten Chemical Mechanical Polishing," Electrochem. Solid-State Lett., **2**(8), pp. 401–403.